

Available online at www.sciencedirect.com

ScienceDirect

journal homepage: www.elsevier.com/locate/hydro

Mechanical behavior of electrochemically hydrogenated electron beam melting (EBM) and wrought Ti–6Al–4V using small punch test

Noa Lulu-Bitton^{a,b}, Eyal Sabatani^b, Brian A. Rosen^a, Natalie Kostirya^b, Gennadi Agronov^b, Eitan Tiferet^{b,c}, Noam Eliaz^{a,*}, Nissim U. Navi^{b,**}

^a Department of Materials Science and Engineering, Tel-Aviv University, Ramat Aviv, Tel Aviv 6997801, Israel

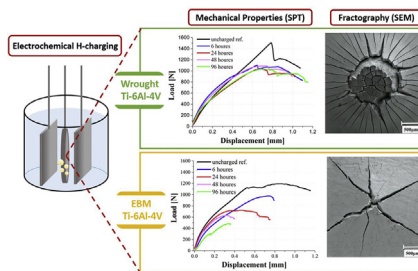
^b Nuclear Research Center Negev (NRCN), P.O. Box 9001, Beer Sheva 84190, Israel

^c AM Center, Rotem Industries Ltd., Mishor Yamin 86800, Israel

HIGHLIGHTS

- Hydrogen effects on electron beam melting (EBM) and wrought Ti–6Al–4V are compared.
- Electrochemical hydrogenation and the small punch test (SPT) are employed.
- The EBM alloy is more susceptible to hydrogen embrittlement than the wrought alloy.
- The fracture mode changes dramatically due to exposure to hydrogen.
- Different hydrogen effects arise from different microstructures and oxygen content.

GRAPHICAL ABSTRACT



ARTICLE INFO

Article history:

Received 12 August 2021

Received in revised form

25 November 2021

Accepted 29 November 2021

Available online 23 December 2021

Keywords:

Additive manufacturing (AM)

Electron beam melting (EBM)

ABSTRACT

The influence of electrochemical charging of hydrogen at $j = -5 \text{ mA/cm}^2$ for 6, 12, 48 and 96 h on the structural and the mechanical behavior of wrought and electron beam melting (EBM) Ti–6Al–4V alloys containing 6 wt% β and similar impurities level was investigated. The length of the α/β interphase boundaries in the EBM alloy was larger by 34% compared to that in the wrought alloy. The small punch test (SPT) technique was used to characterize the mechanical behavior of the non-hydrogenated and hydrogenated specimens. It was found that the maximum load and the displacement at maximum load of the wrought alloy remained nearly stable after 6 h of charging, showing a maximum decrease of ~32% and 11%, respectively. Similarly, hydrogenation of the EBM alloy resulted in a gradual degradation in mechanical properties with charging time, up to ~81% and 86% in pop-in

* Corresponding author.

** Corresponding author.

E-mail addresses: neliaz@tau.ac.il (N. Eliaz), NissimN@nrcn.gov.il (N.U. Navi).

<https://doi.org/10.1016/j.ijhydene.2021.11.231>

0360-3199/© 2021 Hydrogen Energy Publications LLC. Published by Elsevier Ltd. All rights reserved.

Ti–6Al–4V alloy
 Titanium hydride
 Hydrogen embrittlement (HE)
 Small punch test (SPT)

load and displacement at the “pop-in” load, respectively. The mode of fracture of the wrought alloy changed from ductile to semi-brittle with mud-cracking in all hydrogenated specimens. In contrast, the mode of fracture of the EBM alloy changed from a mixed mode ductile-brittle fracture to brittle fracture with star-like morphology. The degraded mechanical properties of the EBM alloy are attributed to its α/β lamellar microstructure which acted as a short-circuit path and enhanced hydrogen diffusion into the bulk as well as δ_a and δ_b hydride formation on the surface. In contrast, a surface layer with higher concentration of δ_a and δ_b hydrides in the wrought alloy served as a barrier to hydrogen uptake into the bulk and increased the alloy resistivity to hydrogen embrittlement (HE). This study shows that EBM Ti–6Al–4V alloy is more susceptible to mechanical degradation due to HE than wrought Ti–6Al–4V alloy.

© 2021 Hydrogen Energy Publications LLC. Published by Elsevier Ltd. All rights reserved.

Introduction

Titanium alloys are used extensively in aerospace applications such as compressor disks, jet engine blades, and airframe structures, mainly due to their superior specific strength [1]. The most commonly used titanium alloy is the dual-phase $\alpha+\beta$ Ti–6Al–4V alloy. The extra-low interstitials (ELI) grade 23, with extra-low concentrations of O, C, N, and H, is commonly used in medical applications such as bone implants [2]. The 6 wt% aluminum stabilizes the α phase while the 4 wt% vanadium stabilizes the β phase. At room temperature (RT), the microstructure at equilibrium consists mainly of the α phase (hcp) with some retained β phase (bcc). A variety of microstructural combinations can be achieved through thermo-mechanical processing. The cooling rate controls the β phase content. For slow cooling rates from high up in the $\alpha+\beta$ region or above the β transition temperature, the β phase transforms mainly to globular α phase. Increasing the cooling rate promotes the α phase nucleation rate at the β grain boundaries, thereby promoting the formation and growth of α platelets into the prior β grains. In this case, the microstructure is bi-lamellar, in which the retained β phase is lying between the α phase grains in a Widmanstätten structure, itself containing thinner secondary α phase platelets [3]. Therefore, the alloy's mechanical properties and corrosion resistance are influenced by the content and morphology of the α and β phases and the density of α/β interfaces [4–7].

Over the years, Ti–6Al–4V alloy was manufactured by traditional techniques such as casting, machining, forging, and powder metallurgy (P/M). In the last decade, however, additive manufacturing (AM) techniques, such as electron beam melting (EBM), selective laser melting (SLM) and directed energy deposition (DED) have become attractive due to the improved efficiency of production. While applying the new AM techniques the parts are subjected to repeated liquid-solid and solid-state phase transformations, rapid solidification, and directional cooling which affect their microstructure [8,9]. Lewandowski and Seifi [10] summarized the mechanical properties of AM Ti–6Al–4V alloys compared to forged, wrought, and annealed Ti–6Al–4V alloys. According to tensile test results, all AM alloys had equal or higher yield strength

and ultimate tensile strength compared to forged/wrought and annealed alloys, but also smaller elongation.

Hydrogen alloying of Ti based alloys is sometimes used to improve the manufacturability and properties of the metal by processes known as thermo-hydrogen processing (THP) or thermo-hydrogen treatment (THT) [4,11–13]. On the other hand, hydrogen is known to embrittle many metals and alloys [14]. Ti and its alloys are sensitive to hydrogen-induced damage, in particular to hydrogen embrittlement (HE) by the hydride formation mechanism [14,15]. This sensitivity can be affected by hydrogen charging conditions, crack tip loading force, and microstructure. In addition, it can be related to the significant differences in diffusivity and solubility of hydrogen in the α (hcp) and β (bcc) phases [16–21]. Thus, in alloys with a high β phase content, hydrogen can diffuse fast through the β phase and react with α phase at interphase boundaries. Solid solution of hydrogen in Ti alloys induces strain due to expansion of the α and β phases lattice parameters [17]. In addition, hydrogen can lead to the formation of hydride phases, such as δ (fcc), ϵ (fct, $c/a < 1$), and γ (fct, $c/a > 1$) [17,19,21–26]. Thus, in dual-phase alloys with high β phase content, hydrogen can diffuse fast through the β phase and react with the α phase at interphase boundaries. The mechanism of local hydride nucleation and growth at α/β interphases was discussed by Kim et al. in Refs. [27–29].

Ti–6Al–4V alloys processed by AM have a different microstructure compared to that of the wrought alloy. Therefore, the susceptibility to HE of AMed alloys could be expected to differ from that of the counterpart wrought alloys. Yet, only a few studies have been performed to-date on hydrogen interaction with AMed Ti–6Al–4V [20,21,26,30–38]. For example, Pushilina et al. [20,30] showed that hydrogen absorption at 500 °C is sensitive to production conditions. Phase transitions and microstructure evolution in EBM Ti–6Al–4V alloy due to gaseous hydrogenation at 650 °C was also reported [21]. The influence of post heat treatment at 750 °C for 1 h in vacuum on the hydrogen sorption rate was studied in Ref. [31]. Laptev et al. [35] investigated the influence of gaseous hydrogenation on defect structure, hardness, and wear resistance of EBM Ti–6Al–4V.

Hydrogen effects on electrochemically charged EBM and wrought Ti–6Al–4V alloys with a similar β phase contents

were investigated by Navi et al. [34]. The EBM alloy was found more susceptible to HE compared to the wrought alloy. A higher density of the α/β interphase boundaries and the discontinuous arrangement of β particles in the EBM alloy promoted both hydride and microvoids formation as well as cracking along the interphase boundaries. In addition, the surface of the hydrogenated alloys consisted of α/α_H (hcp) and β_H (bcc) solid solutions, in addition to δ_a and δ_b hydrides that transformed from the original α phase. It was later reported by the same group [38] that the δ_b hydride was more stable than the δ_a hydride. Microvoids formation in electrochemically charged Ti–6Al–4V [34,39] was attributed by Brosh et al. [39] to hydride precipitation from a hydrogen-supersaturated alloy. Silverstein et al. [26] studied the effect of hydrogen gaseous charging on the hydrogen trapping energy in SLM Ti–6Al–4V and found that the susceptibility to HE depended significantly on the printing direction. Metalnik et al. [33] studied the influence of both gaseous and electrochemical hydrogen charging on EBM Ti–6Al–4V in comparison to the wrought alloy. In the EBM alloy, hydrides were formed after either electrochemical (γ -TiH and δ -TiH_x) or gaseous (δ -TiH_x) charging. Yet, no cracks were observed in the EBM samples after hydrogenation, while hydrogenation of wrought Ti–6Al–4V resulted in severe cracking. Metalnikov et al. [37] investigated the differences between EBM and SLM Ti–6Al–4V alloys in terms of microstructure, hydrogen trapping, and hydrogen evolution. Electrochemical hydrogenation resulted in both cases in a slight increase of the lattice parameters of the α/α' and β phases due to solute hydrogen. The hydrogenated SLM alloy contained both γ and δ hydrides, whereas the EBM alloy contained γ and δ_b hydrides. It was concluded that SLM Ti–6Al–4V with its α' -martensite microstructure was more susceptible to hydride precipitation and hydrogen-assisted cracking (HAC) due to higher tendency for hydrogen absorption and hydride precipitation. In EBM Ti–6Al–4V with its fine duplex $\alpha+\beta$ microstructure, HAC was also observed. HE of AM'ed Ti–6Al–4V has been claimed based on micro-cracking that appeared in metallography cross-sections [26,33,34,37]. Furthermore, Kacenska et al. [40] showed larger deterioration in the mechanical properties (based on tensile tests) of electrochemically hydrogenated SLM Ti–6Al–4V compared to its wrought counterpart due to higher amount of hydrogen absorbed in the SLM alloy. Neikter et al. [41] reported lower resistance to fatigue crack growth of EBM'ed Ti–6Al–4V compared to its wrought counterpart when exposed to high-pressure hydrogen environment.

The static mechanical properties of Ti and its alloys have been measured mainly by traditional techniques such as tensile or compression. However, new techniques have been developed during the last four decades. The small punch test (SPT) [42–44], ball punch test (BPT) [45], disk bend test (DBT) [46], and shear punch test [47,48] were developed in the 1980s especially for nuclear applications.

SPT, specifically, was developed for characterization of the mechanical behavior of structural materials using small or thin specimens. In the SPT, a thin sheet-like specimen is locked between two dies, and a spherical cap-punch is pushed against it until failure. During the test, both the load and the punch stroke are monitored simultaneously until the end-test criterion (e.g., maximal or failure load, a certain stroke, etc.) is

attained. The typical load-displacement curve of ductile materials contains four zones, as described in Ref. [49]: I – elastic behavior, II – plastic behavior (strain hardening), III – plastic membrane stretching, and IV – plastic instability. Specimen rupture is semicircular in shape, and its deflection is high. In contrast, in semi-brittle or brittle materials the membrane stretching zone (III) in the load-displacement curve does not exist, and the transition is from yielding plastic behavior directly to the final plastic instability. In this case, the fracture morphology is *star-like*, and specimen deflection is lower compared to that of ductile materials [50]. Such *star-like* fracture was reported by Arroyo et al. for Cr–Ni–Mn high-strength steel [50], and by Eliaz et al. for amorphous Fe–Si–B alloy [51]. In some cases, the load-displacement curve displays discontinuous load drops (“pop-in” phenomenon) and subsequent increase of the load caused by crack initiation and subsequent crack arrest, as described by Altstadt et al. [52]. On the other hand, a significant load drop (a sharp drop to zero) is indication of crack propagation to final failure. The advantages of the SPT include small specimen dimensions that enable to extract samples directly from the components of interest, and 2D/3D loading profile as compared to uniaxial loading in tensile testing. In addition, with respect to hydrogen or radiation damage, the distribution of hydrogen atoms or radiation damage in the cross-section is more uniform compared to tensile test specimens.

Several researchers [53–57] have studied the effect of hydrogen on the mechanical behavior of steels using SPT. This technique was found exceptionally sensitive to changes in mechanical properties and fracture due to different hydrogen charging conditions. In light of these findings, it was concluded that SPT is a very useful tool for characterization of the mechanical behavior and properties of metals exposed to hydrogen.

It seems that only few studies have been reported on SPT of AM'ed Ti–6Al–4V alloys. Lucon et al. [58] investigated the mechanical properties of EBM Ti–6Al–4V in different metallurgical conditions, namely the as-built condition and after a variety of heat treatments following hot isostatic pressure (HIP). The SPT curves contained one or more load-drop, or “pop-in”, before or after maximum load. In addition, a very low empirical correlation between tensile mechanical properties (yield and ultimate stresses, strain, etc.) and the SPT conditions were found. It was concluded that the SPT has limited applicability to highly anisotropic materials. Lewis et al. [59] employed small punch fatigue (SPF) tests using a single or dual indenter system to compare the fatigue performance of forged, cast and HIP'ed, and EBM Ti–6Al–4V alloys. The SPF technique was found to have a clear sensitivity to identifying the fatigue performance of the tested materials. The EBM alloy exhibited a superior response fatigue behavior due to its fine grain structure. Illsley et al. [60] employed the SPT and demonstrated reduced RT ductility of EBM Ti–6Al–4V compared to both cast and HIP'ed and forged alloy (yet, phase compositions were not reported). In addition, the tested specimens exhibited a mixed-mode fracture, i.e., a combination of ductile and brittle behavior reflected by “star-like” fracture.

The mechanical behavior of Ti–6Al–4V alloys that were manufactured by traditional processes (e.g., casting, forging,

or rolling) and were exposed to hydrogen is well studied [61,62]. In contrast, that of hydrogenated AM'ed Ti–6Al–4V alloys have almost not studied. Gaddam et al. [36] investigated the influence of hydrogen environment on the tensile and low-cycle fatigue (LCF) properties of EBM and cast Ti–6Al–4V alloys. The EBM alloy showed higher tensile strength and LCF properties comparable with those of the cast alloy, both in hydrogen and in air environments. The α -phase colony size was reported as being the most important microstructural feature affecting the tensile strength and LCF properties.

To date, no study has been reported on the effect of electrochemical hydrogenation on the mechanical properties of EBM Ti–6Al–4V alloy compared to its counterpart wrought alloy. Here, such a comparison is made, focusing on the effect of charging time. SPT and scanning electron microscopy (SEM) were employed to study the hydrogen effects on the mechanical properties and mode of fracture, while the temperature-programmed desorption (TPD) technique was used to analyze the content of absorbed hydrogen.

Materials and methods

EBM and wrought Ti–6Al–4V alloys sample preparation

A tray of Ti–6Al–4V samples was manufactured at the AM Center of Rotem Industries Ltd. (Mishor Yamin, Israel) using an Arcam Q20 Plus EBM machine and a standard Grade 5 spherical powder with a size distribution of 45–106 μm . Rod specimens 11 mm in diameter were orientated on the XY plane of the tray. Printing parameters were set to accelerating voltage of 60 kV, beam current of 28 mA, speed function of 32 (~2400 mm/s base beam speed), and layer thickness of 90 μm . The temperature was maintained in the range of 750–850 $^{\circ}\text{C}$. A chamber pressure of 4×10^{-3} mbar was regulated utilizing a helium leak valve.

Wrought Ti–6Al–4V Grade 23 (ASTM F136) rod, 11 mm in diameter, was produced by Dynamet, Inc. The material certificate of the commercial wrought material claimed Ti–6Al–4V Grade 23 (ASTM F136) alloy, annealed at 1300 $^{\circ}\text{F}$ (705 $^{\circ}\text{C}$) for 2 h and air cooled. Samples with a thickness of 0.7 mm were cut by electric discharge machining (EDM), mechanically ground to a thickness of 0.5 mm, and polished on both sides down to 1 μm . The sample's surface was activated by immersing the polished samples in a solution of 2.5 N HNO_3 and 20 g/L NaF for 5 s, followed by rinsing in distilled water. This activation solution is a mild version of the well-known Kroll's reagent, commonly used as an etchant to reveal the microstructure of Ti alloys [34].

Electrochemical hydrogenation

Electrochemical hydrogenation was done galvanostatically ($j = -5 \text{ mA}/\text{cm}^2$) in a three-electrode cell at RT for 6, 24, 48, and 96 h. The Ti–6Al–4V sample served as the cathode, and was placed between two parallel flat anodes made of Pt foils. The electrolyte was H_3PO_4 :glycerin (1:2 vol) [34,38,39,63,64]. The electrolyte was purged with Ar for 30 min prior to charging, and then Ar was kept flowing above the electrolyte during

charging to prevent oxygen absorption. A fresh electrolyte was used for each charging experiment.

Material characterization

Chemical composition and density

The carbon, oxygen, nitrogen, and hydrogen contents were measured by CS–800 carbon analyzer and ONH–2000 oxygen/nitrogen/hydrogen analyzer, respectively (Eltra GmbH, Haan, Germany). Also, the chemical composition of the major elements of the as-received alloys was confirmed by energy-dispersive X-ray spectroscopy (EDS) analysis. The specific gravity of the non-hydrogenated alloys was measured by the Archimedes method, using deionized (DI) water at RT.

Microstructural analysis by SEM and X-ray diffraction (XRD)

The microstructure was characterized using SEM (Quanta 200 FEG ESEM) combined with an EDS detector (Oxford X-Max SDD). Sample preparation for metallographic characterization included mechanical grinding and polishing down to 1 μm , followed by chemical etching in Kroll's reagent (10 mL HF, 30 mL HNO_3 , 50 mL H_2O) [65]. Samples were coated with a thin Au layer to enhance imaging. The β -phase particles area fraction and relative perimeter length were determined from SEM micrographs, using the ImageJ freeware program [66]. The perimeter reflects the surface area of the α/β interface.

XRD at RT was used for phase identification and to determine phase content and lattice parameters. XRD measurements were performed using a D8 ADVANCE diffractometer with a Bragg-Brentano geometry (Bruker AXS, Madison, WI, USA) and Cu-K α radiation source ($\lambda = 1.5418 \text{ \AA}$). A linear position sensitive device (PSD) detector (LYNXEYE XE-T) was used, with an opening of 2.94 $^{\circ}$. Data points were acquired at increments of 0.02 $^{\circ}$ and acquisition time of 0.25 s. The scan was within the range of $2\theta = 20\text{--}100^{\circ}$, though information is presented herein within the range of 33–45 $^{\circ}$ to emphasize major changes. The lattice parameters and phase content were fitted based on Rietveld refinement using TOPAS software, ver. 5 (Bruker AXS, Madison, WI, USA), fitting for the zero-error, lattice parameters and phase composition. NIST Si 640e and LaB6 660c standard reference materials were used to calibrate for peak position and peak shape, respectively. Peaks were fitted using a TCHZ function type, and the U, W, V and the asymmetry parameters were measured using LaB6 660c and fixed to account for instrumental contributions to peak shape.

Desorption analyses using TPD mass spectrometry (TPD-MS)

The total amount of hydrogen trapped in the hydrogenated alloys was determined using TPD-MS apparatus, also known as thermal desorption spectroscopy (TDS). Following the SPT, a typical TPD sample (two duplicates) with a mass of ~18 mg was cut from the SPT specimen's edge, i.e., the zone that is less affected by the SPT measurement. Prior to each TPD measurement, the apparatus was calibrated for quantitative hydrogen analysis using a standard of TiH_2 powder (Sigma Aldrich, 98% purity), which contains a stoichiometric amount of hydrogen (4 wt%) [67]. The TPD apparatus was programmed to heat the tested specimen from RT to 950 $^{\circ}\text{C}$ at a constant rate

of 20 °C/min under a 50 mL/min flow of high-purity He. Procedures for data analysis of TPD are explained in Refs. [64,68], while examples for the use of our homemade system [69,70] as well as the use of TPD/TDS method related to hydrogenate Ti-based alloys can be found elsewhere [25,26,34,71].

Mechanical testing by SPT and micro-hardness

SPTs were performed on wrought and EBM non-hydrogenated and hydrogenated, 0.5 mm thick, Ti–6Al–4V samples. A 2.4 mm diameter hard steel ball was used. The apparatus used for these tests has been described in detail in Refs. [43,44]. The SPT was conducted according to the following steps: (1) clamp the specimen between the dies under 2500 N; (2) preload up to 30 N and balance the stroke transducer (Instron's linear variable differential transducer, LVDT); (3) push the ball into the specimen under stroke control at a speed of 0.1 mm/min to failure. The relative slow rate was chosen in order to better capture any possible effects of hydrogen on the SPT curve in the early stages (Zones I and II in the SPT curve). For each test, the maximum load (F_{max}) was reached, and the experiment was stopped after the load was decreased to 80% of the maximal load, in order to preserve the general features of the deformation and possible cracking. It was reported in Ref. [34] that no change in the XRD patterns of electrochemically hydrogenated samples that were stored for 126 days was observed. It thus seems that the time between the end of the electrochemical hydrogenation and the SPT should not be a critical parameter. Therefore, all SPTs were performed up to 2 months after hydrogenation. After specimen failure, the fracture mode was characterized by SEM.

Vickers micro-hardness tests were conducted on the surface of non-hydrogenated and hydrogenated samples, under 500 g load for 15 s. Prior to testing, a standard block was used to verify the calibration of the testing machine. At least eight indents were analyzed on each sample. Statistical analysis of the micro-hardness results was carried out using analysis of variance (ANOVA) model, with $p < 0.05$ being considered statistically significant.

Results

Chemical composition and density

The concentrations of the impurities in the non-hydrogenated alloys are listed in Table 1. It is evident from Table 1 that oxygen is the main impurity in both alloys, its content in the wrought alloy being higher by 260 wppm (0.026 wt%) than that

in the EBM'd alloy. However, the total impurities contents in both alloys are similar due to the higher nitrogen content in the EBM alloy. The contents of the major elements in both wrought and EBM Ti–6Al–4V alloys were confirmed by EDS. The EBM alloy was found to contain 88.5 wt% Ti, 7.7 wt% Al, and 3.8 wt% V, while the wrought alloy contained 88.4 wt% Ti, 7.8 wt% Al, and 3.8 wt% V. The average densities of the EBM and wrought alloys were 4.421 ± 0.001 and 4.428 ± 0.001 g/cm³, respectively.

Microstructure

Electrochemical charging experiments were performed in the transverse orientation of the samples. Therefore, the results presented herein will be focused on this orientation. SEM micrographs of non-hydrogenated wrought and EBM alloys are shown in Fig. 1a–c and Fig. 1d–f, respectively. Fig. 1a and b shows the wrought alloy in transverse cross-section while Fig. 1c shows the longitudinal orientation. The microstructure of both alloys consists of two phases – α and β (further discussed in Section XRD phase analysis). High-magnification images revealing the morphologies of both phases morphology are shown in Fig. 1b,e. The β phase appears brighter than the α phase and is characterized by higher vanadium content (EDS analysis, see Table 2, points 2 and 4), as expected, since vanadium is known to be a β phase stabilizer. The major gray areas are assigned to the α phase (Table 2, points 1 and 3).

The microstructure of the wrought alloy in the transverse and longitudinal orientations looks different than that in the transverse cross-section. One can see that the β phase morphology in the transverse orientation is discontinuous along the equiaxed α phase boundaries (Fig. 1a,b), while in the longitudinal orientation the β phase texture looks aligned and more continuous, probably due to an extrusion process. A similar microstructure was reported elsewhere [72,73].

The microstructure of the EBM alloy (Fig. 1d–f) is different than that of the wrought alloy. The α and β phases are arranged in a lamellar, Widmanstätten microstructure. The structure is mainly α phase with small amount of β phase within the prior β columnar grains oriented along the build direction. The β phase is discontinuous as a result of rapid solidification in the EBM process, which generates more α/β interfaces in comparison to the wrought alloy. This morphology is typical of EBM Ti–6Al–4V [20,72–74]. The morphology in the longitudinal direction of the EBM alloy (Fig. 1f) is similar to that of the transverse morphology (Fig. 1d). Measurement of the fractional particle area of the β phase (from Fig. 1b,e) indicated a similar content of about 6% in both alloys, in agreement with the content reported in Ref. [34]. The relative perimeter length was measured considering 30 particles in each alloy (similar results were obtained for 20 particles). The total β -particle perimeter (i.e. the α/β interphase length) was found to be larger by 34% in the EBM alloy compared to the wrought alloy.

The microstructures of the wrought and EBM alloys after 96-h hydrogenation are shown in Fig. 2 (Fig. 2a,c,e – wrought alloy, Fig. 2b,d,f – EBM alloy). It can be seen that both alloys, contain a surface layer with a thickness of ~20 μ m or ~35 μ m, respectively, which is attributed to hydride phases. The

Table 1 – Impurity concentrations (wt%) in the non-hydrogenated EBM and wrought Ti–6Al–4V alloys ($n = 6$ for C, O and N; $n = 4$ or 5 for H in the wrought and EBM alloys, respectively).

Element	Wrought	EBM
C	0.0066 ± 0.0005	0.0063 ± 0.0002
O	0.1352 ± 0.0318	0.1092 ± 0.0175
H	0.0036 ± 0.0006	0.0036 ± 0.0004
N	0.0052 ± 0.0011	0.0322 ± 0.0025
Total	0.1506 ± 0.0340	0.1513 ± 0.0206

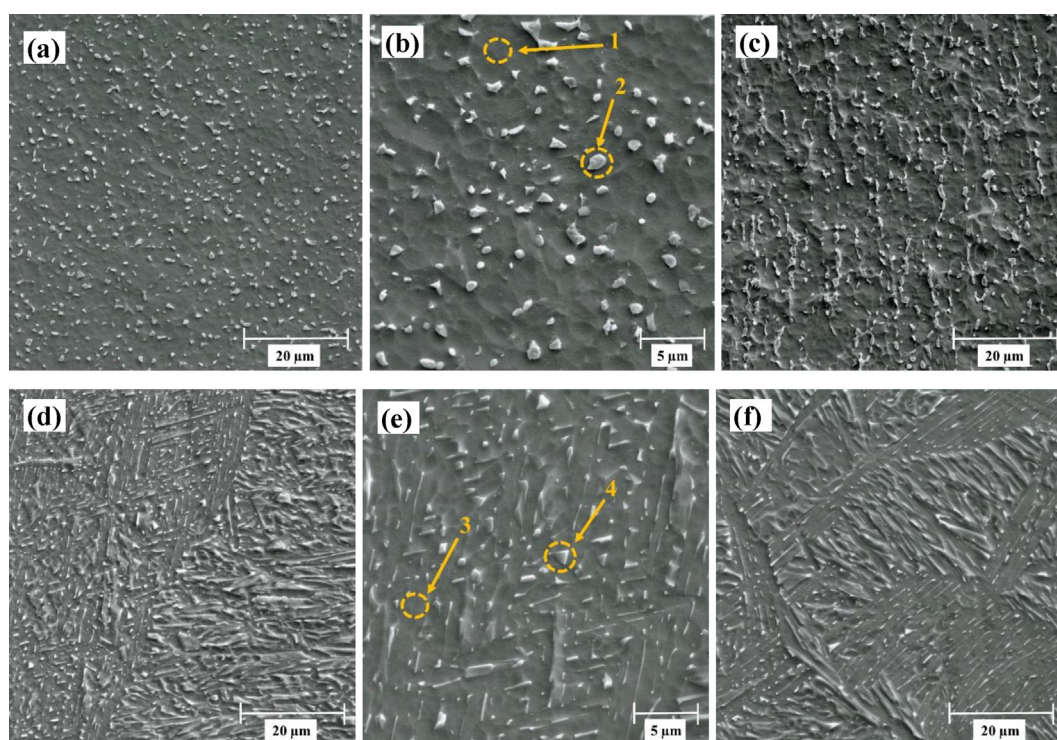


Fig. 1 – SEM secondary electrons (SE) images in the transverse cross-sections of the wrought (a,b) and EBM (d,e) alloys and in the longitudinal cross-sections of the wrought (c) and EBM (f) alloys. The arrows in the figures point on local EDS analyses of Ti, Al, and V as listed in Table 2.

Table 2 – Local EDS chemical composition (wt%) in non-hydrogenated EBM and wrought Ti–6Al–4V alloys.

Sample	Ti	Al	V
Wrought, point 1 in Fig. 1b	88.9	7.7	3.4
Wrought, point 2 in Fig. 1b	82.9	7.0	10.1
EBM, point 3 in Fig. 1e	89.7	7.6	2.7
EBM, point 4 in Fig. 1e	81.6	5.8	12.6

morphology of the hydride layer in the wrought alloy (Fig. 2c) is characterized by hydrides with a stripe morphology and several microvoids, while the morphology of the hydride layer in the EBM alloy (Fig. 2d) is characterized by clusters of hydrides (marked by red circle), also accompanied by some microvoids. Microvoid formation in Ti–6Al–4V following electrochemical hydrogenation in a similar electrolyte was observed in Refs. [34,39], and has been attributed to hydride precipitation from a hydrogen-supersaturated alloy [39]. In addition, the original morphology of both alloys (namely, the α/β interfaces) seems to be either masked or diminished by the hydride formation, and is therefore not seen in the layer. The microstructure beneath the hydride layers in both alloys (Fig. 2e and f) is similar to that in the non-hydrogenated alloys. It should be emphasized that in both hydrogenated alloys no macro-cracks were observed.

XRD phase analysis

Normalized XRD patterns (maximal peak is 100%) of the non-hydrogenated and the hydrogenated wrought and EBM alloys

are shown in Fig. 3. Fig. 3a (the ordinate values are after arbitrary shift) shows the phases in the wrought alloy as a function of hydrogenation time. The non-hydrogenated sample contains two phases – α (major) and β (minor). The β phase content as measured by XRD was about 6 wt%, in agreement with the value of the fractional area of β phase that was measured based on SEM micrographs (see Section Microstructure).

After hydrogenation, the wrought alloy contains β_H solid solution and both δ_a and δ_b hydride phases, that are variants of δ (TiH_x) phase. These hydrides have fcc unit cell and space group $Fm\bar{3}m(225)$. They were first reported by Navi et al. [34], and were later reported also in Refs. [38,39]. Table 3 and Table 4 show the phase contents and lattice parameters calculated by TOPAS Rietveld refinement (all values of R_{wp} were below 11.64). The c/a ratio of the major α phase in the non-hydrogenated wrought alloy (calculated from the data in Tables 3 and 4) is higher than that in the EBM'ed alloy – 1.599 and 1.596, respectively, indicating a larger degree of distortion in the wrought alloy. The δ_a and δ_b phases evolved after 6-h hydrogenation, and their content increased from 0 to 40–47 wt% (each phase, see Table 3), and then remained nearly constant over charging time. Moreover, after 6-h charging, the α phase disappeared and the β phase content increased from 6 to 11–14 wt% (Table 3). It can be seen in Fig. 3a that the non-hydrogenated (110) β peak at $2\theta = 39.8^\circ$ shifts to a lower reflection angle ($2\theta = 38.9^\circ$) after 96-h hydrogenation, reflecting an increase in the lattice parameter from $a = 3.194$ to 3.269 \AA (i.e., an increase of 23%) due to the formation of β_H solid solution.

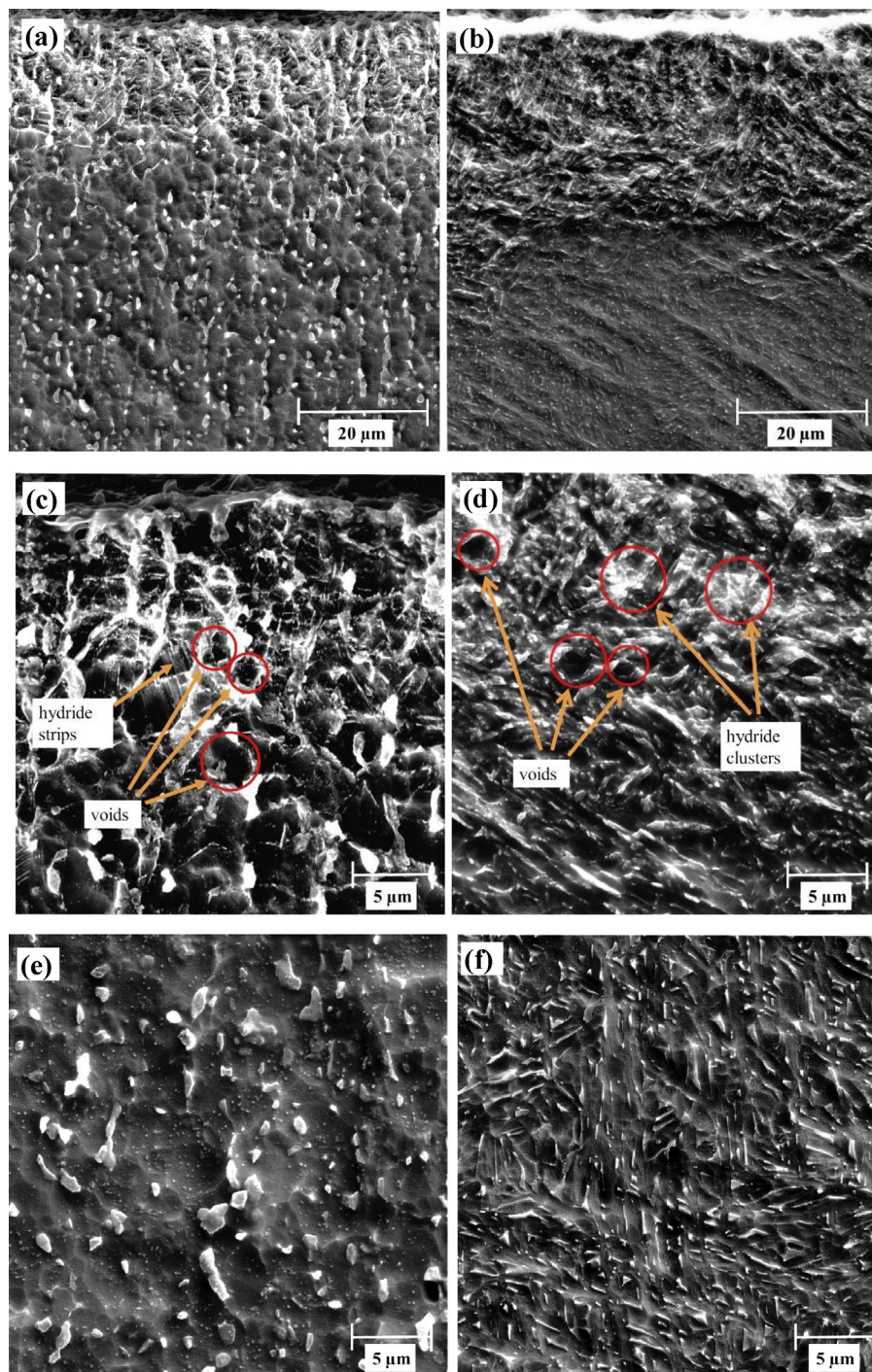


Fig. 2 – SEM SE images revealing the hydride layer in metallographic cross-sections of 96-h hydrogenated wrought (a,c,e) and EBM (b,d,f) alloys.

Normalized XRD patterns of the non-hydrogenated and hydrogenated EBM alloys are shown in Fig. 3b (the ordinate values are after arbitrary shift). It is seen that the phase change as a function of charging time is different from that in the wrought alloy. The α phase content gradually decreased from 93 to 4 wt% after 96-h hydrogenation (i.e., α did not disappear completely as in the wrought alloy, see Table 4) and its peak position did not change due to hydrogenation, indicating that its lattice parameters remained essentially

constant during hydrogenation. This can be explained by the low solubility of hydrogen in the α phase [16–21,34]. The total content of δ_a and δ_b hydrides was ~45% after 6 and 24 h of hydrogenation due to α phase transformation into δ_a and δ_b hydrides [34,38]. Their total content increased to ~85% after 48 and 96 h of hydrogenation, simultaneously with a further decrease in the α phase content. The β_H peaks are broadened after 6 and 24 h of hydrogenation, presumably due to nano-domains formation, as discussed in Ref. [38]. The lattice

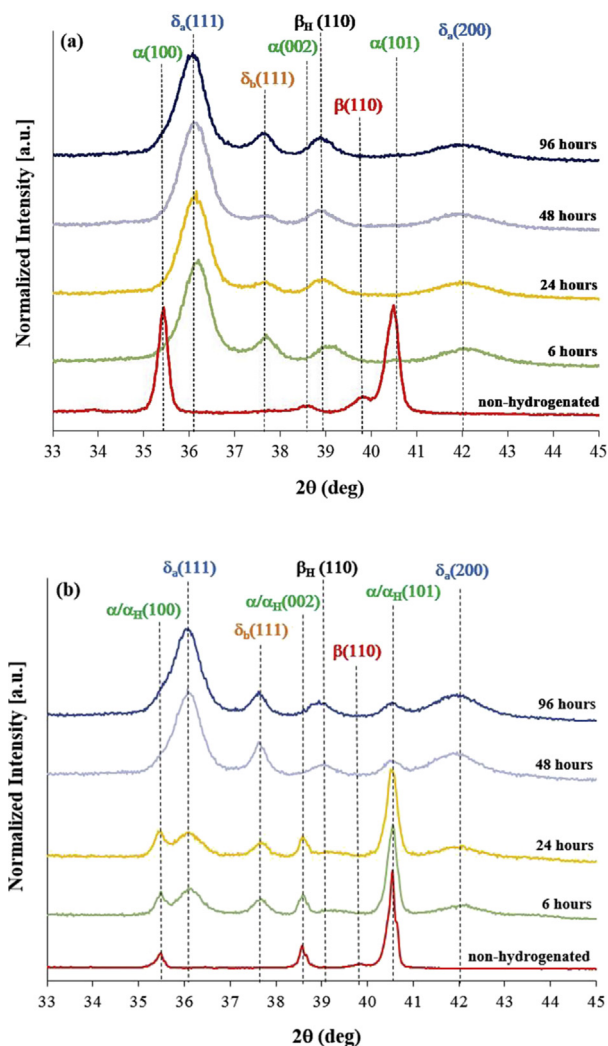


Fig. 3 – XRD patterns of non-hydrogenated and 6, 24, 48, and 96 h hydrogenated wrought (a) and EBM (b) Ti–6Al–4V alloys. The ordinates' values are after an arbitrary shift.

parameter of the cubic β phase increased from $a = 3.198 \text{ \AA}$ to $a = 3.251 \text{ \AA}$, an increase of 16.5% and less than the growth percent in the wrought alloy. The β_H phase content increased from 6 wt% (as β phase) to ~14 wt% after 96-h hydrogenation (Table 4), similar to the observation for the wrought alloy. It

can be seen from Table 4 that the phase contents after 6 and 24 h of charging are similar, so are the phase contents after 48 and 96 h of charging. This may be attributed to kinetic aspects that were not investigated in this study.

TPD analysis

The total amount of desorbed hydrogen (H_2 , wppm) as a function of charging time in both alloys is shown in Fig. 4. The average hydrogen content in the wrought alloy was ~780 wppm after 6-h hydrogenation, and then increased to ~3100 wppm after 24-h hydrogenation and remained constant until 96-h hydrogenation, i.e., no major absorption of hydrogen occurred in the wrought alloy from 24-h charging on. This indicates that the hydrogen uptake reached a steady state. In contrast, the average hydrogen content in the EBM alloy after 6-h hydrogenation was ~1070 wppm, and gradually increased with charging time up to ~6000 wppm after 96 h. In addition, one can see that the total amount of hydrogen in the EBM alloy was larger than in the wrought alloy at any charging time.

Micro-hardness and SPT curves

The Vickers micro-hardness values of the non-hydrogenated and hydrogenated alloys are shown in Fig. 5. The non-hydrogenated wrought and EBM samples have similar micro-hardness, which is lower than that of the hydrogenated samples. The micro-hardness of the wrought alloy (Fig. 5a) increases by 26% up to a charging time of 24 h, and then stabilizes with further charging, in agreement with the TPD data. In contrast, the micro-hardness of the EBM alloy (Fig. 5b) increases gradually by 32%, shows a maximum after 48 h, and then decreases with further charging to 96 h.

SPT curves and SEM top view images of the fracture zone in non-hydrogenated and hydrogenated wrought and EBM alloys are shown in Fig. 6. Higher-magnification images of fractures are shown in Figs. 7 and 8. It is evident from Fig. 6 that the mechanical behavior of the four types of samples is different. The non-hydrogenated wrought alloy (Fig. 6a) has a SPT curve typical of ductile material behavior. In contrast, the non-hydrogenated EBM SPT curve (Fig. 6b) is typical of mixed ductile-brittle materials that do not have a membrane stretching zone (zone III) and transit from yielding plastic behavior directly to the final plastic instability. In addition, the EBM SPT curve contains a load drop (“pop-in” phenomenon) at

Table 3 – Lattice parameters and phase contents in the non-hydrogenated and hydrogenated wrought alloy.

	α/α_H	β/β_H	δ_a	δ_b
Non-hydrogenated	94.41 wt%	5.59 wt%	–	–
	$a = 2.925 \text{ \AA}$, $c = 4.678 \text{ \AA}$	$a = 3.194 \text{ \AA}$		
6-h hydrogenation	–	13.78 wt%	45.59 wt%	40.63 wt%
		$a = 3.255 \text{ \AA}$	$a = 4.306 \text{ \AA}$	$a = 4.144 \text{ \AA}$
24-h hydrogenation	–	15.29 wt%	44.74 wt%	39.97 wt%
		$a = 3.271 \text{ \AA}$	$a = 4.314 \text{ \AA}$	$a = 4.154 \text{ \AA}$
48-h hydrogenation	–	15.65 wt%	44.57 wt%	39.78 wt%
		$a = 3.276 \text{ \AA}$	$a = 4.314 \text{ \AA}$	$a = 4.154 \text{ \AA}$
96-h hydrogenation	–	10.71 wt%	47.31 wt%	41.98 wt%
		$a = 3.269 \text{ \AA}$	$a = 4.315 \text{ \AA}$	$a = 4.146 \text{ \AA}$

Table 4 – Lattice parameters and phase contents in the non-hydrogenated and hydrogenated EBM alloy.

	α/α_H	β/β_H	δ_a	δ_b
Non-hydrogenated	93.54 wt% $a = 2.924 \text{ \AA}, c = 4.668 \text{ \AA}$	6.46 wt% $a = 3.198 \text{ \AA}$	–	–
6-h hydrogenation	47.65 wt% $a = 2.926 \text{ \AA}, c = 4.670 \text{ \AA}$	6.19 wt% $a = 3.247 \text{ \AA}$	24.44 wt% $a = 4.308 \text{ \AA}$	21.72 wt% $a = 4.142 \text{ \AA}$
24-h hydrogenation	46.68 wt% $a = 2.928 \text{ \AA}, c = 4.668 \text{ \AA}$	5.86 wt% $a = 3.245 \text{ \AA}$	25.15 wt% $a = 4.313 \text{ \AA}$	22.32 wt% $a = 4.145 \text{ \AA}$
48-h hydrogenation	6.58 wt% $a = 2.927 \text{ \AA}, c = 4.605 \text{ \AA}$	9.65 wt% $a = 3.254 \text{ \AA}$	44.42 wt% $a = 4.308 \text{ \AA}$	39.36 wt% $a = 4.138 \text{ \AA}$
96-h hydrogenation	4.02 wt% $a = 2.917 \text{ \AA}, c = 4.597 \text{ \AA}$	13.81 wt% $a = 3.251 \text{ \AA}$	43.57 wt% $a = 4.294 \text{ \AA}$	38.60 wt% $a = 4.125 \text{ \AA}$

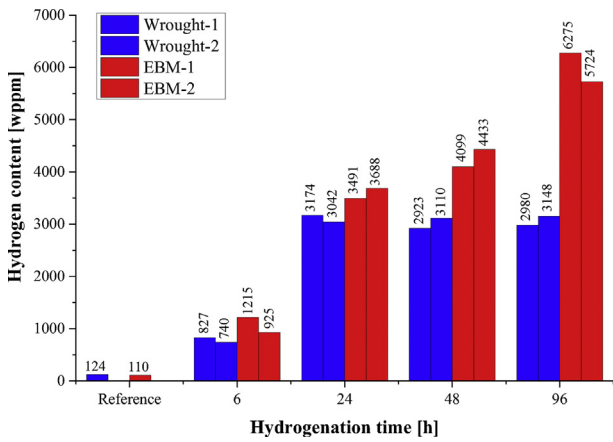


Fig. 4 – Total amount of absorbed hydrogen in the wrought (blue) and EBM (red) specimens charged for 6, 24, 48, and 96 h, based on TPD analysis. A duplicate was tested from each alloy after each charging time. (For interpretation of the references to colour in this figure legend, the reader is referred to the Web version of this article).

~1100 N, before the maximum is reached. The load drop may indicate local failure in the matrix, such as crack initiation followed by crack arrest. Similar SPT values (P_{max} , δ_{max}) and curve shape were reported before [58,60]. It should be emphasized that for the wrought alloy, the maximum load (P_{max}) and displacement at maximum load (δ_{max}) values are the maximal values in the SPT curve, In contrast, for the EBM alloy, these values are represented by the first pop-in event, i.e., P_{pop-in} load and δ_{pop-in} displacement associated with damage.

After hydrogenation, the mechanical properties of both alloys deteriorate. For the wrought alloy, the mechanical behavior can be divided into two groups – uncharged versus hydrogenated (Fig. 6a). The mechanical behavior of all EBM samples degrade gradually with charging time, showing a pop-in phenomenon that indicate a brittle behavior (Fig. 6b).

SEM fractography of the wrought alloy after SPT is shown in Fig. 7. The uncharged wrought alloy (Fig. 7a–c) exhibits a typical ductile fracture, which contains dimples, as clearly evident at high magnification in Fig. 7c. The fracture also contains shearing zones (Fig. 7b), similar to those described by Valoppi et al. after incremental sheet forming (ISF) process [75]. Hydrogenation generates a thin hydride layer with a

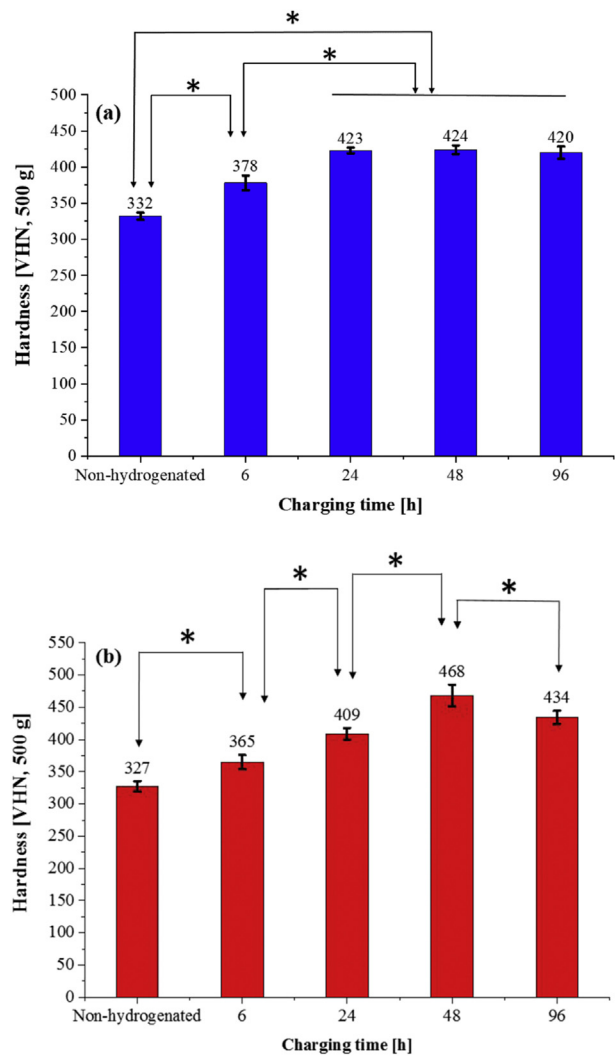


Fig. 5 – Micro-hardness of non-hydrogenated and hydrogenated wrought (a) and EBM (b) Ti–6Al–4 alloy. * denotes $p < 0.05$, i.e., statistical significance.

thickness of ~12 μm after 6 h (not shown here), and ~35 μm beyond 24 h (Fig. 7e,h). This layer contains β_H , δ_a and δ_b phases, as shown by the XRD data above. This layer does not contain dimples, thus indicating a brittle character (Fig. 7f,i). As a result, tensile stresses developing under the ball during

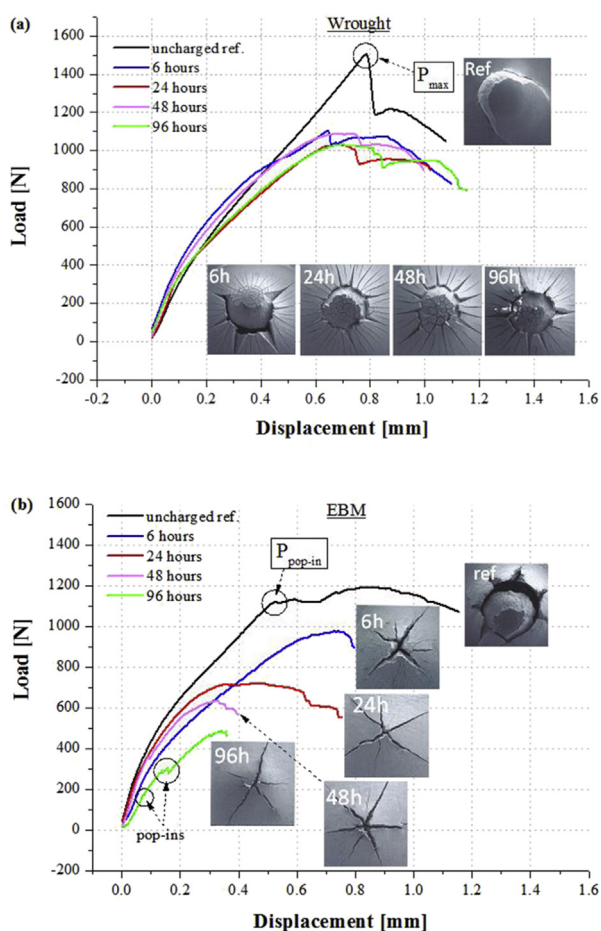


Fig. 6 – SPT curves of non-hydrogenated and hydrogenated wrought (a) and EBM (b) Ti-6Al-4V alloys. Insets: SEM fracture images.

the SPT result in a combination of circular and radial cracks, known as “mud-cracks” (Fig. 7d,g). These cracks propagate through the entire layer and arrest at the interface between the brittle layer and the ductile underlying alloy (Fig. 7e,h). Such a mud-crack fracture morphology was described by Seghir and Arscott in thin film metallization of chromium/gold on polydimethylsiloxane (PDMS) [76], as well by Eliaz for hard chromium coatings on steel [77].

The fractography of the EBM alloy after SPT is shown in Fig. 8. The uncharged specimen exhibits a mixed-mode (ductile and brittle) fracture behavior (Fig. 8a) despite the dimples that evident on the fracture surface (Fig. 8b and c). This mixed-mode fracture is manifested by a combination of circular crack shape and star-like features, which is characteristic of failure of brittle materials in SPT. This type of fracture was reported by Illsley et al. after SPT of EBM Ti-6Al-4V [60]. At all charging times, the mode of fracture is only star-like, as shown in Fig. 8d,g. The EBM macro-fracture contains primary cracks, which form the star-like morphology, and secondary cracks that emanate from the primary cracking origin, which stopped growing when the catastrophic failure occurred. During the test, the primary cracks grow to their final size until final failure. High-

magnification images revealing the fracture's surface morphology after 24 and 96 h of charging are shown in Fig. 8e,f,h,i. It can be seen that for both charging times the fracture is apparently interlamellar [78] which progressively evolved during the test.

To summarize the SPT results, the load (P_{\max} , $P_{\text{pop-in}}$) and displacement (δ_{\max} , $\delta_{\text{pop-in}}$) as a function of hydrogenation time for the two alloys are shown in Fig. 9. It is evident from Fig. 9a that P_{\max} and $P_{\text{pop-in}}$ of the wrought alloy are always higher than those of the EBM alloy. The maximum load of the wrought alloy decreases from ~1400 N (non-hydrogenated) to 1100 N after 6-h hydrogenation, with no major changes in the maximum load after 24 and 48 h of charging. The maximum load drops to a minimum of ~950 N after 96 h of hydrogenation (an overall decrease of ~32% in load). For the EBM alloy, the first pop-in load decreases gradually from ~1100 N (non-hydrogenated) to 200 N after 96 h of hydrogenation (an overall decrease of ~81% in load).

From Fig. 9b it is evident that the displacement as a function of hydrogenation time of the wrought alloy was higher than that of the EBM alloy for most conditions. The displacement of the wrought alloy was relatively stable and decreases by only ~11%, from ~0.69 to 0.61 mm, whereas for the EBM alloy the displacement decreased gradually up to 48 h of hydrogenation, from ~0.52 to 0.07 mm (~86%), and stabilized with further charging time. The decrease in load and displacement of both alloys is an indication of their increased embrittlement due to hydrogenation. In this regards, the EBM alloy is found to be more prone to HE than the wrought alloy.

Discussion

The influence of electrochemical hydrogenation at $j = -5 \text{ mA/cm}^2$ in a glycerin-based acidic solution on the microstructure and mechanical properties of wrought and EBM Ti-6Al-4V alloys containing ~6 wt% β was investigated. The similar content of the β phase in both alloys allowed to eliminate (fractional) phase effects on its susceptibility to hydrogen embrittlement (HE). The amount of α/β interphase boundaries in the EBM'd alloy is larger by 34% compared to the wrought alloy. The mechanical properties of non-hydrogenated Ti-6Al-4V alloys are known to be influenced by many parameters [10], such as phase content and morphology [79,80], impurities content, and lattice strain [81]. For the non-hydrogenated alloys, the oxygen content in the wrought alloy is higher by 0.026 wt% than in the EBM'd alloy. According to Ref. [81], it is expected that such difference in oxygen concentration (assuming that all other parameters in both alloys are similar) would lead to an increase in the α phase degree of distortion (i.e., c/a ratio) by ~0.0003. However, it was indicated above that the degree of distortion of α in the wrought alloy increased by ca. 0.003, i.e. by a factor of 10 higher than expected. Therefore, since the impurity levels in both non-hydrogenated alloys were similar, we can conclude that the impurities content in the two alloys (including oxygen) did not play a significant role in the degree of distortion difference between the two alloys. In addition, due to the similar phase content and densities of both alloys we may conclude that the differences in the degree of distortion and microstructure of

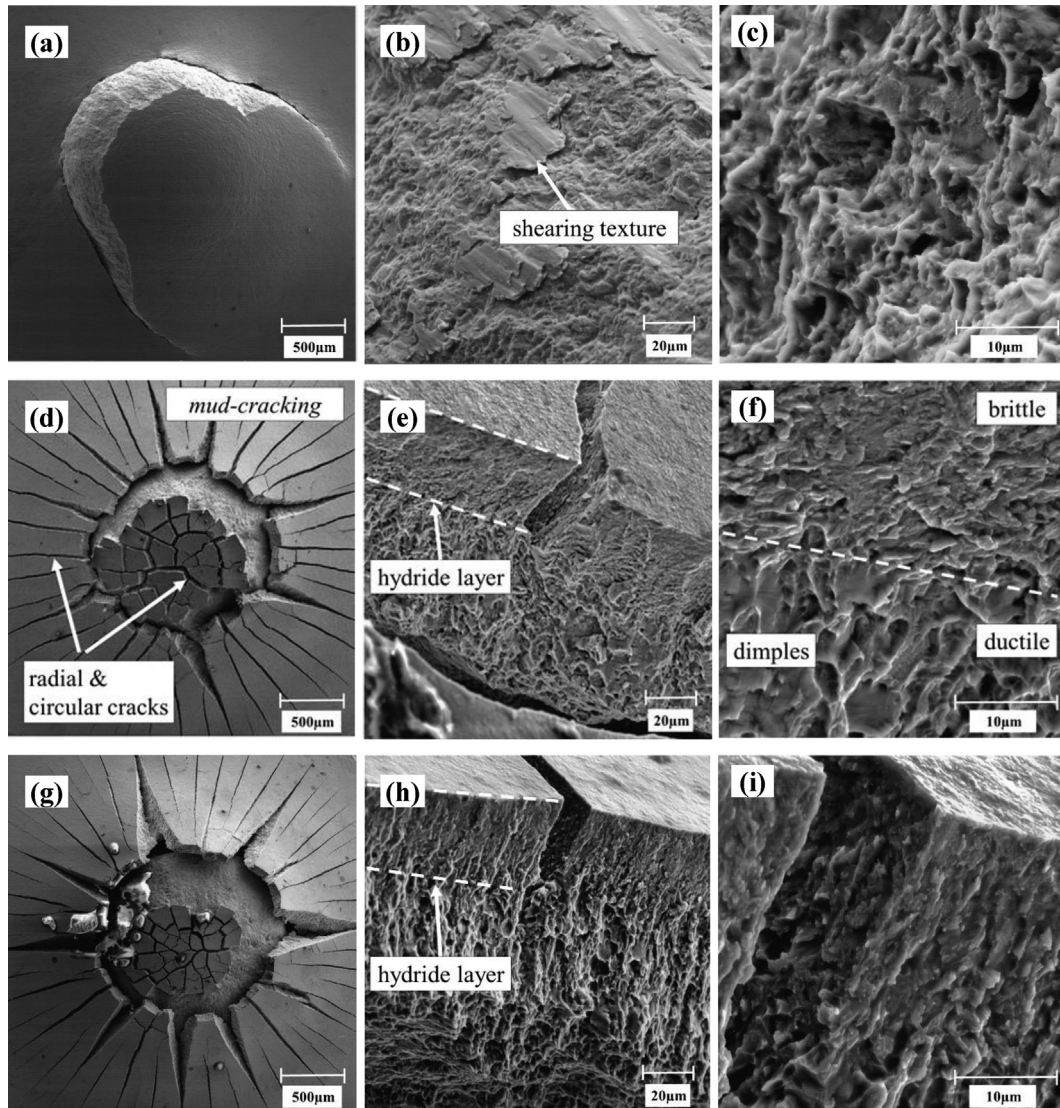


Fig. 7 – SEM fractography of wrought Ti–6Al–4V alloy after SPT. (a–c) non-hydrogenated, (d–f) 24 h charging, (g–i) 96 h charging.

both alloys are responsible for their different mechanical properties and behavior.

After 6-h hydrogenation, the α phase in the wrought alloy disappeared and was replaced by high content of δ_a and δ_b hydrides (~86 wt% in total). At the same time, the β_H content increased from 6 wt% to ~15 wt% due to the tendency of hydrogen to stabilize the β phase in Ti alloys [62]. The phase composition did not change with further hydrogenation time. The presence of δ_a and δ_b hydrides along with β_H is in agreement with a previous report of Navi et al. [34]. The total hydrogen content in the wrought alloy increased up to ~3000 wppm after 24-h hydrogenation and did not change at longer hydrogenation times. The micro-hardness of the wrought alloy that increased up to 24 h did not change significantly further with increasing hydrogenation time. The load and displacement at failure were decreased by ~32% and 11%, respectively, showing a relative constant mechanical behavior versus charging time. The mode of fracture of the wrought alloy changed due to hydrogenation from ductile to semi-

brittle fracture for all hydrogenation times, showing a mud-crack morphology. Thus, it can be concluded that the wrought alloy reached steady state in all terms of phase contents, hydrogen content, and mechanical properties within 6–24 h charging. This may be attributed to the formation of a surface layer that inhibited further hydrogen diffusion into the bulk and prevented further hydrogen-induced damage. This finding is supported by Hruška et al. [82] who found that the diffusion of hydrogen through the δ hydride layer is sluggish, therefore the kinetics of full hydrogenation is slowed down.

In contrast, in the EBM alloy, the α phase content reduced gradually and the contents of the δ_a and δ_b hydrides increased, from ~45 wt% in total after 6-h hydrogenation to 81 wt% after 96-h hydrogenation. The total hydrogen content in the EBM alloy increased progressively up to ~6000 wppm. The SPT load and displacement at the first pop-in also decreased gradually, by ~81% and 86%, respectively. The SPT mode of fracture changed from mixed-mode fracture (ductile-brittle) to brittle

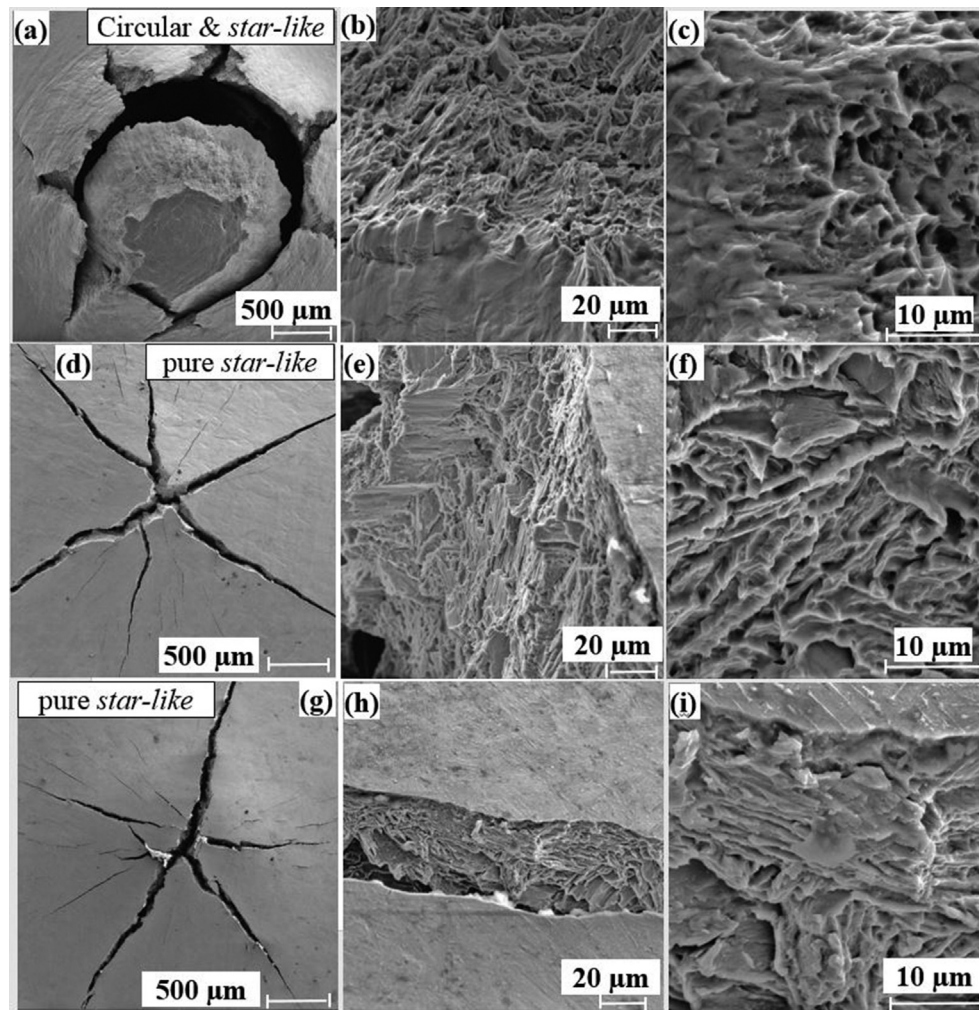


Fig. 8 – SEM fractography of EBM Ti–6Al–4V alloy after SPT. (a–c) non-hydrogenated, (d–f) 24 h charging, (g–i) 96 h charging.

fracture with star-like morphology. Thus, it can be concluded that the EBM alloy degraded progressively as a function of charging time and was more prone to hydrogen-induced damage than the wrought alloy. The differences in the alloys' sensitivity to hydrogen damage can be attributed to their different microstructures. The wrought alloy is characterized by reduced hydrogen diffusion paths due to equiaxed α phase and discontinuous β phase morphology with relatively smaller number of α/β interphase boundaries. On the other hand, the Ti–6Al–4V EBM alloy, which also contains discontinuous β phase, is characterized by a higher density of α/β interphase boundaries arranged in a lamellar Widmanstätten microstructure. Hence, the microstructure of the EBM alloy contains significantly more short-circuit paths for fast hydrogen diffusion, which enhances hydrogen ingress and transport through the material [83].

The hydrogen content in both alloys was similar up to 24 h charging time, although the β_{H} phase contents in the EBM and in the wrought alloys were ~6 wt% and ~15 wt%, respectively. Since the diffusivity and solubility of hydrogen in β -Ti are higher than in α -Ti [16–21], it could be expected that the

content of hydrogen in the wrought alloy will be higher than that in the EBM alloy. This discrepancy can be attributed to three factors: (1) higher density of α/β interfaces in the EBM alloy, which act as short-circuit paths for hydrogen diffusion, (2) the presence of a hydride surface layer with higher concentration of the δ_{a} and δ_{b} hydrides in the wrought alloy, which further inhibits hydrogen diffusion into the bulk, and (3) higher solute oxygen content in the wrought alloy (see Table 2) that decreases the hydrogen solubility in titanium at a fixed pressure, as reported by Yamanaka et al. [84–86]. Although we cannot distinguish between the effect of these three factors on the hydrogen content in each alloy, we believe that the difference in density of the α/β interphase boundaries in the two alloys, which also affects the hydride formation at the surface, is more significant.

The higher hydrogen uptake of the EBM alloy compared to that of the wrought alloy and the disappearance of the α phase from the wrought alloy after hydrogenation are in apparent disagreement with the previous observations of Navi et al. [34]. However, in the previous study a higher current density of $j = -25 \text{ mA/cm}^2$ was employed, the oxygen content in the

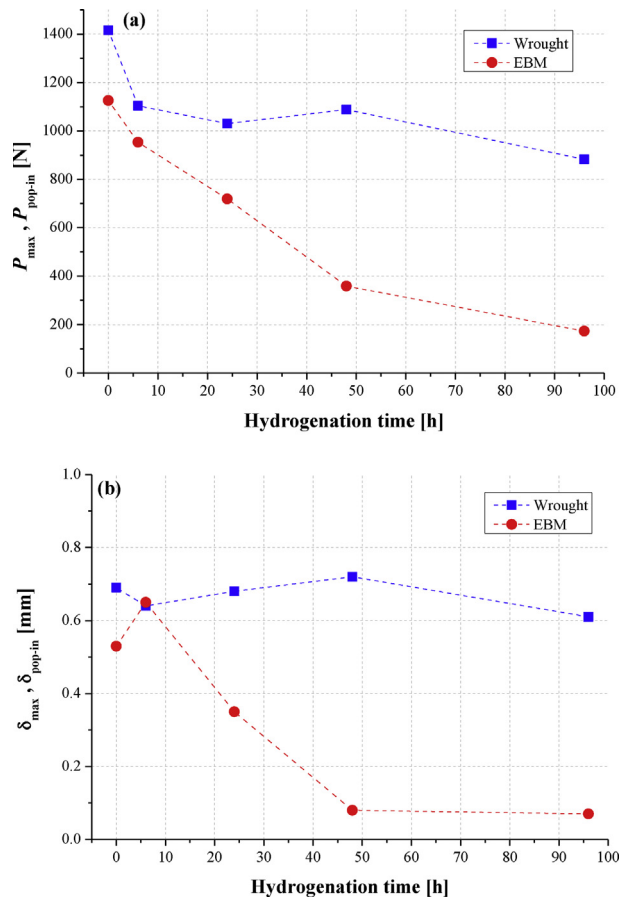


Fig. 9 – (a) Load (P_{\max} and $P_{\text{pop-in}}$), and (b) displacement (δ_{\max} and $\delta_{\text{pop-in}}$) from SPT curves for wrought and EBM Ti–6Al–4V alloys.

EBM alloy was higher than in the wrought alloy, and the microstructure of the wrought alloy was different. In this study, the microstructure of the wrought alloy consisted of equiaxed α phase and discontinuous β phase along the α phase grain boundaries, while the microstructure of the wrought alloy in Ref. [34] consisted of large, elongated grains of α phase and a lamellar α/β structure in between, which enhanced hydrogen uptake. We believe that the above three differences are responsible for a different kinetic behavior.

Conclusions

The influence of electrochemical hydrogenation on the microstructure and mechanical behavior of electron beam melting (EBM) additively manufactured (AM'ed) and wrought Ti–6Al–4V alloys containing 6 wt% β was studied. The main conclusions are listed below:

1. The degradation in mechanical properties as a function of charging time of the EBM alloy was more significant compared to the wrought alloy due to microstructural differences. The EBM alloy was more susceptible to hydrogen embrittlement than the wrought alloy.

2. Higher density of α/β interphase boundaries that are contained in a lamellar Widmanstätten microstructure in the EBM alloy combined with lower oxygen content promoted the higher susceptibility to hydrogen embrittlement of the EBM alloy.
3. A surface layer with higher concentration of δ_a and δ_b hydrides in the wrought alloy served as a barrier for hydrogen uptake into the bulk, thus further contributing to the increased resistance of the wrought alloy to hydrogen embrittlement.
4. The mode of fracture of the EBM alloy changed from a mixed-mode (ductile and brittle) fracture to brittle star-like fracture at longer hydrogen charging times.
5. The mode of fracture of the wrought alloy changed from ductile to semi-brittle with mud-cracks due to hydrogenation.

Declaration of competing interest

The authors declare that they have no known competing financial interests or personal relationships that could have appeared to influence the work reported in this paper.

Acknowledgements

This work was supported by grant No. 322/20 from the Pazy Foundation of the Israel Atomic Energy Commission and the Israeli Council of Higher Education. We thank Dr. Shlomo Haroush for advising on the SPT tests, Mr. Nadav Guy for gas analysis, Mr. David Hai David and Mr. Maymon Cohen for technical assistance, Mr. Michael Chonin and Mr. Yaron I. Ganor for EBM of Ti–6Al–4V, and Mr. David Noiman for density measurements.

REFERENCES

- [1] Boyer RR. An overview on the use of titanium in the aerospace industry. *Mater Sci Eng A* 1996;213:103–14.
- [2] Eliaz N. Corrosion of metallic biomaterials: a review. *Materials* 2019;12:407.
- [3] Lutjering G. Influence of processing on microstructure and mechanical properties of $\alpha+\beta$ titanium alloys. *Mater Sci Eng A* 1998;243:32–45.
- [4] Eliezer D, Eliaz N, Senkov ON, Froes FH. Positive effects of hydrogen in metals. *Mater Sci Eng A* 2000;280:220–4.
- [5] Paramore JD, Fang ZZ, Dunstan M, Sun P, Butler BG. Hydrogen-enabled microstructure and fatigue strength engineering of titanium alloys. *Sci Rep* 2017;7:41444.
- [6] Ding R, Guo ZX, Wilson A. Microstructural evolution of a Ti6Al4V alloy during thermomechanical processing. *Mater Sci Eng A* 2002;327:233–45.
- [7] Kohn DH, Ducheyne P. Microstructural refinement of β -sintered and Ti-6Al-4V porous-coated by temporary alloying with hydrogen. *J Mater Sci* 1991;26:534–44.
- [8] Zhai Y, Galarraga H, Lados DA. Microstructure, static properties, and fatigue crack growth mechanisms in Ti-6Al-

- 4V fabricated by additive manufacturing: LENS and EBM. *Eng Fail Anal* 2016;69:3–14.
- [9] Kok Y, Tan XP, Wang P, Nai MLS, Loh NH, Liu E, Tor SB. Anisotropy and heterogeneity of microstructure and mechanical properties in metal additive manufacturing: a critical review. *Mater Des* 2018;139:565–86.
- [10] Lewandowski JJ, Seifi M. Metal additive manufacturing – a review of mechanical properties. *Annu Rev Mater Res* 2016;46:151–86.
- [11] Eliaz N, Eliezer D, Olson DL. Hydrogen-assisted processing of materials. *Mater Sci Eng A* 2000;289:41–53.
- [12] Zong Y, Wu K. Thermo hydrogen treatment for microstructure refinement and mechanical properties improvement of Ti-6Al-4V alloy. *Mater Sci Eng A* 2017;703:430–7.
- [13] Losertová M, Hartmann M, Schindler I, Drápala J. Hydrogen treatment of titanium-based alloys. *Mater Sci Eng* 2017;266:012007.
- [14] Eliaz N, Gileadi E. *Physical electrochemistry: fundamentals, techniques, and applications*. 2nd ed. Weinheim, Germany: Wiley-VCH; 2019. Ch. 17.
- [15] Madina V, Azkarate I. Compatibility of materials with hydrogen. Particular case: hydrogen embrittlement of titanium alloys. *Int J Hydrogen Energy* 2009;34:5976–80.
- [16] Fukai Y. *The metal-hydrogen system*. New York, USA: Springer-Verlag; 1993. p. 22.
- [17] Luo L, Su Y, Guo J, Fu H. Formation of titanium hydride in Ti-6Al-4V. *J Alloys Compd* 2006;425:140–4.
- [18] Blackburn JL, Parilla PA, Gennett T, Hurst KE, Dillon AC, Heben MJ. Measurement of the reversible hydrogen storage capacity of milligram Ti-6Al-4V alloy samples with temperature programmed desorption and volumetric techniques. *J Alloys Compd* 2008;454:483–90.
- [19] Liu HJ, Zhou L, Liu P, Liu QW. Microstructural evolution and hydride precipitation mechanism in hydrogenated Ti-6Al-4V alloy. *Int J Hydrogen Energy* 2009;34:9596–602.
- [20] Pushilina N, Syrtanov M, Kashkarov E, Murashkina T, Kudiiarov V, Laptev R, Lider A, Koptyug A. Influence of manufacturing parameters on microstructure and hydrogen sorption behavior of electron beam melted titanium Ti-6Al-4V alloy. *Materials* 2018;11:763.
- [21] Pushilina N, Panin A, Syrtanov M, Kashkarov E, Kudiiarov V, Perevalova O, Laptev R, Lider A, Koptyug A. Hydrogen induced phase transformation and microstructure evolution for Ti-6Al-4V parts produced by electron beam melting. *Metals* 2018;8:301.
- [22] Okamoto H. H-Ti (hydrogen-titanium). *J Phase Equilibria Diffus* 2011;32:174–5.
- [23] Wu T-I, Wu J-K. Effects of electrolytic hydrogenating parameters on structure and composition of surface hydrides of CP-Ti and Ti-6Al-4V alloy. *Mater Chem Phys* 2002;74:5–12.
- [24] Sun P, Fang ZZ, Koopman M, Paramore J, Ravi Chandran KS, Ren Y, Lu J. An experimental study of the (Ti-6Al-4V)-xH phase diagram using in situ synchrotron XRD and TGA/DSC techniques. *Acta Mater* 2015;84:29–41.
- [25] Ma M, Liang L, Wang L, Wang Y, Cheng Y, Tang B, Xiang W, Tan X. Phase transformations of titanium hydride in thermal desorption process with different heating rates. *Int J Hydrogen Energy* 2015;40:8926–34.
- [26] Silverstein R, Eliezer D. Hydrogen trapping in 3D-printed (additive manufactured) Ti-6Al-4V. *Mater Char* 2018;144:297–304.
- [27] Kim J, Tasan CC. Microstructural and micro-mechanical characterization during hydrogen charging: an in situ scanning electron microscopy study. *Int J Hydrogen Energy* 2019;44:6333–43.
- [28] Kim J, Plancher E, Tasan CC. Hydrogenation-induced lattice expansion and its effects on hydrogen diffusion and damage in Ti-6Al-4V. *Acta Mater* 2020;188:686–96.
- [29] Kim J, Kang J, Tasan CC. Hydride formation in Ti6Al4V: an in situ synchrotron x-ray diffraction study. *Scripta Mater* 2021;193:12–6.
- [30] Pushilina N, Kudiiarov V, Syrtanov M, Kashkarov E. Effect of the beam current during the electron-beam melting of titanium alloy Ti-6Al-4V on the structural features and phase transitions in gas-phase hydrogenation. *J Surf Investig* 2018;13:429–33.
- [31] Pushilina N, Stepanova EN, Kudiiarov VN, Laptev RS, Syrtanov MS. Heat treatment of the Ti-6Al-4V alloy manufactured by electron beam melting. *AIP Conf Proc* 2019;2167:020290.
- [32] Bilgin GM, Esen Z, Akin SK, Dericioglu AF. Optimization of the mechanical properties of Ti-6Al-4V alloy fabricated by selective laser melting using thermohydrogen processes. *Mater Sci Eng A* 2017;700:574–82.
- [33] Metalnik P, Eliezer D, Ben-Hamu G, Tal-Gutelmacher E, Gelbstein Y, Munteanu C. Hydrogen embrittlement of electron beam melted Ti-6Al-4V. *J Mater Res Technol* 2020;9:16126–34.
- [34] Navi NU, Tenenbaum J, Sabatani E, Kimmel G, Ben David R, Rosen BA, Barkay Z, Ezersky V, Tiferet E, Ganor YI, Eliaz N. Hydrogen effects on electrochemically charged additive manufactured by electron beam melting (EBM) and wrought Ti6Al4V alloys. *Int J Hydrogen Energy* 2020;45:25523–40.
- [35] Laptev R, Kudiiarov V, Pushilina N. Hydrogen influence on defect structure and mechanical properties of EBM Ti-6Al-4V. *Mater Today Proc* 2019;19:2084.
- [36] Gaddam R, Åkerfeldt P, Pederson R, Antti ML. Influence of hydrogen environment on the mechanical properties of cast and electron beam melted Ti-6Al-4V. In: Zhou L, editor. *Ti-2011: proc. 12th world conf on titanium*. Beijing, China: Social Sciences Academic Press; 2012. p. 1885–8.
- [37] Metalnik P, Eliezer D, Ben-Hamu G. Hydrogen trapping in additive manufactured Ti-6Al-4V alloy. *Mater Sci Eng A* 2021;811:141050.
- [38] Navi NU, Rosen BA, Sabatani E, Tenenbaum J, Tiferet E, Eliaz N. Thermal decomposition of titanium hydrides in electrochemically hydrogenated electron beam melting (EBM) and wrought Ti-6Al-4V alloys using in situ high-temperature X-ray diffraction. *Int J Hydrogen Energy* 2021;46:30423–32.
- [39] Brosh E, Navi NU, Rosen BA, Eliaz N. Microvoids in electrochemically hydrogenated titanium-based alloys. *Int J Hydrogen Energy* 2021;46:27234–42.
- [40] Kacenska Z, Roudnika M, Ekrt O, Vojtech D. High susceptibility of 3D-printed Ti-6Al-4V alloy to hydrogen trapping and embrittlement. *Mater Lett* 2021;301:130334.
- [41] Neikter M, Colliander M, Schwerz CDA, Hansson T, Åkerfeldt P, Pederson R, Antti ML. Fatigue crack growth of electron beam melted Ti-6Al-4V in high-pressure hydrogen. *Materials* 2020;13:1287.
- [42] Guduru RK, Wong PZ, Darling KA, Koch CC, Murty KL. Determination of activation volume in nanocrystalline Cu using the shear punch test. *Adv Eng Mater* 2007;9:855–9.
- [43] Haroush S, Priel E, Moreno D, Bussiba A, Silverman I, Turgeman A, Shneck R, Gelbstein Y. Evaluation of the mechanical behavior of the mechanical properties of SS-316L thin foils by small punch testing and finite element analysis. *Mater Des* 2015;83:75–84.
- [44] Haroush S, Moreno D, Bussiba A, Silverman I, Turgeman A, Shneck R, Gelbstein Y. The mechanical behavior of HAVAR foils using the small punch test technique. *Materials* 2017;10:491.

- [45] ASTM E643–87. Standard test method for ball punch deformation of metallic sheet material. West Conshohocken, PA, USA: ASTM International; 1987.
- [46] Manahan M, Browning AE, Argon AS, Harling OK. Miniaturized disk bend test technique development and application. In: Corwin WR, Lucas GE, editors. ASTM STP 888: the use of small-scale specimens for testing irradiated material. West Conshohocken, PA, USA: ASTM International; 1986. p. 17–49.
- [47] Guduru RK, Darling KA, Kishore R, Scattergood RO, Koch CC, Murty KL. Evaluation of mechanical properties using shear-punch testing. *Mater Sci Eng A* 2005;395:307–14.
- [48] Hamilton ML, Toloczko MB. Effect of low temperature irradiation on the mechanical properties of ternary V-Cr-Ti alloys as determined by tensile and shear punch tests. *J Nucl Mater* 2000;283–287:488–91.
- [49] CEN Workshop Agreement, CWA 15627:2007 E. Small punch test method for metallic materials. Brussels: European Committee for Standardisation; 2007.
- [50] Arroyo B, Álvarez JA, Lacalle R, Gutiérrez-Solana F. Rate effects on the estimation of fracture toughness by small punch tests in hydrogen embrittlement scenarios. *Ubiquity Proc* 2018;1(S1):SSTT2018.
- [51] Eliaz N, Moshe E, Eliezer S, Eliezer D. Hydrogen effects on the spall strength and fracture characteristics of amorphous Fe-Si-B alloy at very high strain rates. *Metall Mater Trans A* 2000;31:1085–93.
- [52] Altstadt E, Bergner F, Das A, Houska M. Effect of anisotropic microstructure of ODS steels on small punch test results. *Theor Appl Fract Mech* 2019;100:191–9.
- [53] Garcia TE, Rodriguez C, Belzunze FJ, Penuelas I, Arroyo B. Development of a methodology to study the hydrogen embrittlement of steels by means of the small punch test. *Mater Sci Eng A* 2015;626:342–51.
- [54] Janca A, Siegl J, Hausild P, Levy M. Hydrogen embrittlement of steels studied using small punch test method. *Powder Metall Prog* 2015;15:99–104.
- [55] Arroyo B, Alvarez JA, Lacalle R, Gonzalez P, Solana FG. Using small punch tests in environment under static load for fracture toughness estimation in hydrogen embrittlement. *Mater Sci Eng* 2017;272:012033.
- [56] Snir Y, Haroush S, Danon A, Gelbstein Y, Landau A, Eliezer D. Metallurgical and hydrogen effects on small punch tested mechanical properties of PH-13-8Mo stainless steel. *Materials* 2018;11:1966.
- [57] Snir Y, Haroush S, Dannon A, Landau A, Eliezer D, Gelbstein Y. Aging condition and trapped hydrogen effects on the mechanical behavior of a precipitation hardened martensitic stainless steel. *J Alloys Compd* 2019;805:509–16.
- [58] Lucon E, Benzing JT, Derimow N, Hrabec N. Small punch testing to estimate the tensile and fracture properties of additively manufactured Ti-6Al-4V. *J Mater Eng Perform* 2021;30:5039–49.
- [59] Lewis DTS, Lancaster RJ, Jeffs SP, ILLSLEY HW, Davies SJ, Baxter GJ. Characterising the fatigue performance of additive materials using the small punch test. *Mater Sci Eng A* 2019;754:719–27.
- [60] ILLSLEY H, Lancaster R, Hurst R, Jeffs S, Baxter G. Mechanical property characterisation of electron beam melted (EBM) Ti-6Al-4V via small punch tensile testing. *Key Eng Mater* 2017;734:51–60.
- [61] Tal-Gutelmacher E, Eliezer D. The hydrogen embrittlement of titanium-based alloys. *JOM* 2005;57:46–9.
- [62] Zhou L, Liu HJ. Effect of hydrogenation on microstructure and mechanical properties of Ti-6Al-4V titanium alloy. *Adv Mater Res* 2013;750–752:596–602.
- [63] Kirchheim R, McLellan RB. Electrochemical methods for measuring diffusivities of hydrogen in palladium and palladium alloys. *J Electrochem Soc* 1980; 127:2419–25.
- [64] Eliaz N, Eliezer D, Abramov E, Zander D, Köster U. Hydrogen evolution from Zr-based amorphous and quasicrystalline alloys. *J Alloys Compd* 2000;305:272–81.
- [65] ASTM E407–15. Standard practice for microetching metals and alloys. West Conshohocken, PA, USA: ASTM International; 2015.
- [66] Ferreira T, Rasband W. ImageJ user guide. <http://imagej.nih.gov/ij/docs/guide>. [Accessed 25 November 2021].
- [67] Zeppelin FV, Haluška M, Hirscher M. Thermal desorption spectroscopy as a quantitative tool to determine the hydrogen content in solids. *Thermochim Acta* 2003;404:251–8.
- [68] Verbeken K. Analysing hydrogen in metals: bulk thermal desorption (TDS) methods. In: Gangloff RP, Somerday BP, editors. Gaseous hydrogen embrittlement of materials in energy technologies, vol. 2. Cambridge, UK: Woodhead Publishing Limited; 2012. p. 27–55.
- [69] Ben David R, Bitton N, Simca F, Samuha S, Fadel D, Danon A, Finkelstein Y. Non-isothermal hydrogen desorption from β -UH3: kinetics and mechanism. *J Nucl Mater* 2018;510:484–91.
- [70] Ifergane S, Ben David R, Sabatani E, Carmeli B, Beeri O, Eliaz N. Hydrogen diffusivity and trapping in Custom 465® stainless steel. *J Electrochem Soc* 2018;165:C107–15.
- [71] Ben David R, Finkelstein Y, Nativ-Roth E, Danon A, Cohen D, Rabkin E. The role of surface coarsening and sintering during thermal decomposition of titanium hydride. *Int J Hydrogen Energy* 2019;44:6045–54.
- [72] Mohammad S, Razavi J, Filippo B. Directed energy deposition versus wrought Ti-6Al-4V: a comparison of microstructure, fatigue behavior and notch sensitivity. *Adv Eng Mater* 2019;21:1900220.
- [73] Ganor YI, Tiferet E, Vogel SC, Brown DW, Chonin M, Pesach A, Hajaj A, Garkun A, Samuha S, Shneck RZ, Yeheskel O. Tailoring microstructure and mechanical properties of additively-manufactured Ti6Al4V using post processing. *Materials* 2021;14:658.
- [74] Rafi HK, Karthik NV, Gong H, Starr TL, Stucker BE. Microstructures and mechanical properties of Ti6Al4V parts fabricated by selective laser melting and electron beam melting. *J Mater Eng Perform* 2013;22:3872–83.
- [75] Valoppi B, Zhang Z, Deng M, Ghiotti A, Bruschi S, Ehmann KF, Cao J. On the fracture characterization in double-sided incremental forming of Ti6Al4V sheets at elevated temperatures. *Proced Manufact* 2017;10:407–16.
- [76] Seghir R, Arscott S. Controlled mud-crack patterning and self-organized cracking of polydimethylsiloxane elastomer surfaces. *Sci Rep* 2015;5:14787.
- [77] Eliaz N. High efficiency aeronautical hard chromium platings. *Mater Technol* 2002;17:81–6.
- [78] Yang J, Li H, Hu D, Dixon M. Microstructural characterisation of fatigue crack growth fracture surfaces of lamellar Ti45Al2Mn2Nb1B. *Intermetallics* 2014;45:89–95.
- [79] Hrabec N, Quinn T. Effects of processing on microstructure and mechanical properties of a titanium alloy (Ti–6Al–4V) fabricated using electron beam melting (EBM), part 1: distance from build plate and part size. *Mater Sci Eng A* 2013;573:264–70.
- [80] Hrabec N, Quinn T. Effects of processing on microstructure and mechanical properties of a titanium alloy (Ti–6Al–4V) fabricated using electron beam melting (EBM), part 2: energy input, orientation, and location. *Mater Sci Eng A* 2013;573:271–7.

-
- [81] Oh JM, Lee BG, Cho SW, Lee SW, Choi GS, Lim JW. Oxygen effects on the mechanical properties and lattice strain of Ti and Ti-6Al-4V. *Met Mater Int* 2011;17:733–6.
- [82] Hruška P, Čížek J, Knapp J, Lukáč F, Melikhova O, Mašková S, Havela L, Drahoukoupil J. Characterization of defects in titanium created by hydrogen charging. *Int J Hydrogen Energy* 2017;42:22557–63.
- [83] Aucouturier M. Grain boundary segregations and hydrogen embrittlement. *J Phys Colloq* 1982;43(C6):175–86.
- [84] Yamanaka S, Tanaka T, Tsuboi S, Miyake M. Effect of oxygen on solubility of hydrogen isotopes in titanium. *Fusion Eng Des* 1989;10:303–8.
- [85] Yamanaka S, Ogawa H, Miyake M. Effect of interstitial oxygen on hydrogen solubility in titanium, zirconium and hafnium. *J Less Common Met* 1991;172–174:85–94.
- [86] Yamanaka S, Fujita Y, Uno M, Katsura M. Influence of interstitial oxygen on hydrogen solubility in metals. *J Alloys Compd* 1999;293–295:42–51.